Check for updates

Received: 5 May 2022 | Revised: 7 July 2022 | Accepted: 13 July 2022

DOI: 10.1111/ffe.13797

ORIGINAL ARTICLE

FFEMS Fatigue & Fracture of Engineering Materials & Structures WILEY

Assessment of mechanical and fatigue crack growth properties of wire + arc additively manufactured mild steel components

Muhammad Shamir[1] | **Victor Igwemezie**[2] | **Saeid Lotfian**[1] | **Rhys Jones**[3,4] | **Huzaifa Asif**[5] | **Supriyo Ganguly**[2] | **Ali Mehmanparast**[1]

[1]Department of Naval Architecture, Ocean & Marine Engineering, University of Strathclyde, Glasgow, UK

[2]Welding Engineering and Laser Processing Centre, Cranfield University, Cranfield, UK

[3]Faculty of Mechanical and Aerospace Engineering, Monash University, Clayton, Victoria, Australia

[4]ARC Industrial Transformation Training Centre on Surface Engineering for Advanced Materials, Faculty of Science, Engineering and Technology, Swinburne University of Technology, Hawthorn, Victoria, Australia

[5]Faculty of Materials and Chemical Engineering, GIK Institute of Engineering Sciences and Technology, Swabi, Pakistan

Correspondence
Ali Mehmanparast, Department of Naval Architecture, Ocean & Marine Engineering, University of Strathclyde, Glasgow G1 1XQ, UK.
Email: ali.mehmanparast@strath.ac.uk

Funding information
UK Engineering and Physical Sciences Research Council (EPSRC), Grant/Award Number: EP/S000747/1

Abstract

A study has been conducted to evaluate the mechanical and fatigue crack propagation properties of wire + arc additively manufactured ER70S-6 components. A parallel-built deposition strategy was employed to fabricate the additively manufactured wall. The hardness values were slightly higher at the bottom and top of the wall due to the presence of Widmanstätten ferrite and carbides. The characterization of mechanical properties in both orientations; parallel and perpendicular to the deposition direction showed a marginal difference in yield strength and ultimate tensile strength. The crack growth rates were correlated with linear elastic fracture mechanics parameter ΔK and compared with an oscillation-built deposition strategy from the literature. The crack growth rates of both deposition strategies were found to be very similar to each other. Furthermore, it has been demonstrated that the variability in the crack growth histories can be reasonably well captured by using the NASGRO crack growth equation.

KEYWORDS

additive manufacturing, fatigue crack growth, fracture mechanics, mechanical properties, steel

1 | INTRODUCTION

Additive manufacturing (AM) has received particular attention in recent years due to its significant advantages and widespread applications in the aerospace, biomedical and power sectors.[1–5] One of the most important benefits of AM, compared to traditional manufacturing methods, is the potential for reducing material volume, hence cost saving, during the fabrication process which has attracted significant interest from both industry and academia.[6] Apart from material savings, AM offers the capability to produce complex shapes through layer-by-layer

This is an open access article under the terms of the Creative Commons Attribution License, which permits use, distribution and reproduction in any medium, provided the original work is properly cited.
© 2022 The Authors. *Fatigue & Fracture of Engineering Materials & Structures* published by John Wiley & Sons Ltd.

deposition allowing more design flexibility and significant weight reductions in the parts produced by AM. The wire + arc additive manufacturing (WAAM) is a directed energy deposition (DED) AM process where a wire is fed into an electric or plasma arc heat source at a constant feed rate to build a large near net shape parts.[7,8] The deposition rate of steel by the WAAM process is approximately 10 kg/h with better material utilization as compared to other AM processes.[9,10] Nevertheless, due to higher deposition rates and high heat input, residual stresses and distortions are higher in WAAM components.[11,12]

WAAM has been recognized as one of the most efficient advanced manufacturing technologies for production of large-scale components and structures. In all engineering structures, the load-bearing parts must be designed to be durable and damage tolerant. Durability is related to the economic life of a component under cyclic loads, while damage tolerance is the ability of a structure to safely operate in the presence of defects or cracks until the damage reaches a critical level. Depending on the application, the failure criteria could be based on either crack initiation or crack propagation. Most of the structural components, in the aerospace and power sector, are designed for damage tolerance, that is, based on the crack propagation life from initial crack length to a critical crack size. With continuous development in AM technologies, WAAM is expected to provide a range of new materials for application in the aerospace and power sector. These newly developed processes and materials need to be tested for their durability and damage tolerance. There is limited literature available on the fatigue behavior of WAAM-built low-carbon steels such as ER70S-6.[13–15] A recent study by Ermakova et al.[14,15] was conducted on WAAM-built components made of ER70S-6 using an oscillation-built strategy while Dirisu et al.[16] compared mechanical properties of oscillation and single-pass WAAM ER70S-6. They demonstrated comparable mechanical properties to the conventionally manufactured counterparts.

While the employment of AM technologies has been considered in a number of industries, such as aerospace, the use of WAAM technology in offshore renewable energy applications has received some attention in recent years due to the advantages that the WAAM technology offers for manufacturing and repair purposes.[17] Currently, offshore and onshore wind energy contribute to about 8.1% and 9.1% of the UK's energy generation, respectively, and subsequently the reduction of 12 million tonnes of CO_2.[18] Offshore wind is comparatively a young industry, compared to other well-established energy industries such as oil and gas and nuclear, with a typical design lifetime of 20–25 years. An important way to increase the return on investments in offshore wind industry is to enable life extension for those wind farms which have reached the end of their initial design life.[19] WAAM offers a competitive advantage for the repair and life enhancement of offshore wind turbine support structures due to its low cost and flexibility[9,16] and is expected to have a great potential to support the existing life extension efforts. However, the assessment of structural integrity of WAAM-built layers and components is essential in order to employ this process for life enhancement of offshore wind assets.

The cost-effective materials that can be considered for repair and life enhancement of offshore structures are mild steels which are widely used in various engineering applications and their wrought material properties are characterized in previous research studies. Haden et al.[20] examined the WAAM-built component and wrought steel and found that both have the same bulk hardness while Lu et al.[21] found similar static properties of both wrought and WAAM mild steel. While there are limited number of studies on the structural integrity assessment of WAAM-built components made of mild steels, more research investigations have been carried out by various researchers to study the titanium WAAM-built components for application in aerospace industry. The review of previous studies on titanium WAAM-built components showed that the change in built strategy changes the heat input which results in different microstructures of the final builds.[22,23] A study conducted by Syed et al.[23] showed that because of different heat input in oscillation-built strategy, the yield and tensile strength was lower than parallel-built Ti64 walls. Furthermore, the fatigue strength of oscillation-built Ti64 walls at 10^7 cycles was 500 MPa as compared to 600 MPa in the case of parallel-built walls. On the other hand, the crack growth rates were lower in oscillation-built walls due to lower yield strength (YS) and larger grain size resulting in larger plastic zone sizes ahead of the crack tip and causing crack deflection due to larger grains. Nevertheless, to date, there has been no direct comparison made in the literature on the effect of deposition strategies on fatigue crack growth (FCG) behavior of WAAM-built components made of mild steels. Therefore, the purpose of this research is to investigate the FCG properties of parallel deposited WAAM ER70S-6 and compare them with oscillation deposited pattern available in the literature.

2 | MATERIAL FABRICATION PROCESS

A mild carbon ER70S-6 copper-coated steel wire from Lincoln Electric was used to build a wall using cold metal

transfer (CMT)-based WAAM process. The process parameters are summarized in Table 1. The WAAM wall was built on an EN10025 structural steel base plate with dimensions of 350 × 250 × 12 mm^3. The parallel bead strategy was employed in fabrication of the WAAM wall where four parallel passes were deposited consecutively at a given height along the wall length with a 35% overlap between adjacent passes. The dimensions of each wall were 300 mm in length (L), 150 mm in height (h), and 25 mm in thickness (t). The WAAM setup consisted of a CMT power source, a robot arm with a CMT torch feeding the wire along with the shielding gas nozzle as shown in Figure 1. To extract the heat and fumes generated during the process, an exhaust was placed near the working table. The base plate was clamped to the working table using six clamps to prevent distortion due to thermal residual stresses (see Figure 2A). The clamps were released once the WAAM wall was cooled down. The wall was finally removed from the base plate upon completion of the fabrication process and sample cool down.

TABLE 1 CMT-WAAM fabrication parameters

Shielding gas	Ar + 20% CO_2
Gas flow rate	15 L/min
Robot traveling speed	0.4 m/min
Wire diameter	1.2 mm
Wire feed speed	7.0 m/min
Dwell time	120 s

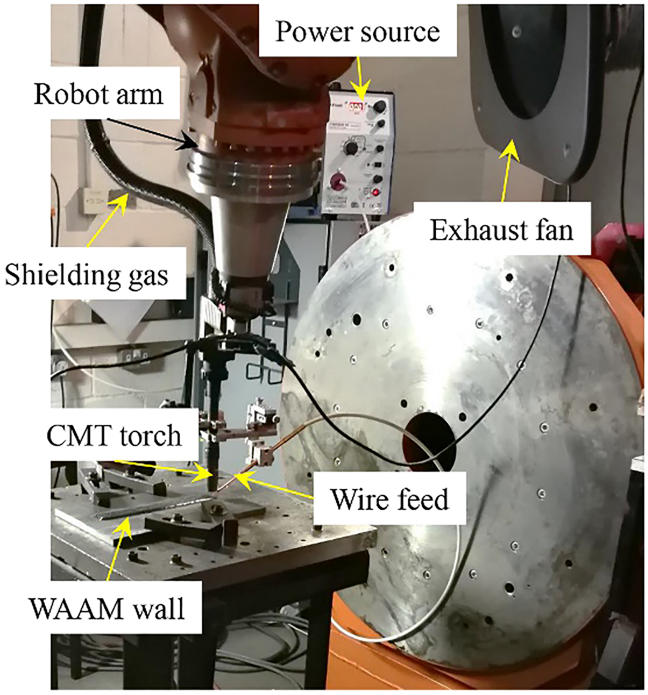

FIGURE 1 CMT-WAAM set up for fabrication of ER70S-6 wall [Colour figure can be viewed at wileyonlinelibrary.com]

Samples were extracted from the WAAM wall for tensile tests, fatigue crack propagation tests, micro-hardness tests and microstructural analysis. Tensile and fatigue crack propagation samples were extracted with two different orientations with respect to the WAAM deposition direction and were classified as "horizontal" and "vertical" samples as shown in Figure 2B. In horizontal tensile samples, the loading direction was parallel to the deposition direction (i.e., parallel to X axis in Figure 2B) while in vertical tensile samples, the loading direction was perpendicular to the deposition direction (i.e., parallel to Z axis in Figure 2B). In horizontal fatigue crack propagation samples, the crack plane was oriented parallel to the deposition direction whereas in vertical samples the crack plane was normal to the deposition direction. The geometry and extraction strategy for all test samples are shown in Figure 2B.

The samples for microstructural analysis were extracted from the as-deposited wall and prepared using Buehler Metaverse 250 grinding and polishing machine. The surface of these samples was ground and etched with 2% Nital solution to reveal the macro and microstructure showing layer interfaces. For microstructure analysis, optical light microscopy and scanning electron microscopy (SEM) were used. The line intercept method, as

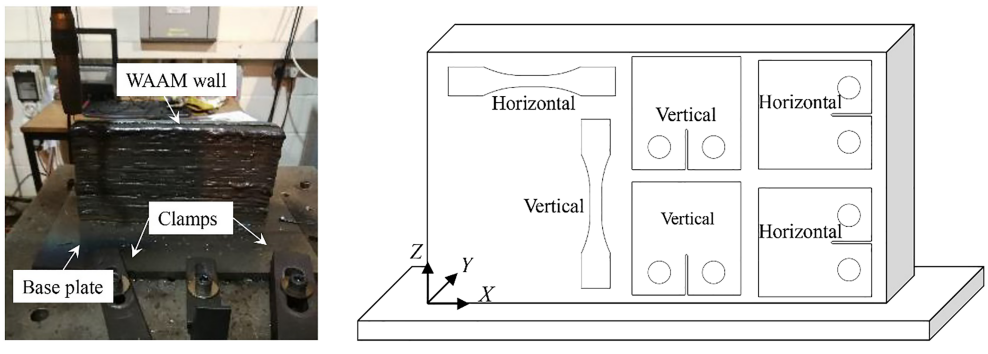

FIGURE 2 (A) CMT-WAAM fabricated ER70S-6 wall and (B) schematic illustration of the extraction plan and specimen orientations [Colour figure can be viewed at wileyonlinelibrary.com]

described in ASTM E1382 standard,[24] was used to measure the grain size. Micro-hardness measurements were carried out according to BS EN ISO 6507-1:1997 standard.[25] The hardness readings were taken along the build direction (*Z* axis in Figure 2B) and along the wall thickness (*Y* axis in Figure 2B) with an incremental distance of 2 mm.

The tensile samples were designed according to the ASTM E8 standard.[26] Three tensile tests for each orientation (i.e., horizontal and vertical directions) were conducted using a 100 kN servo-hydraulic test machine. The tests were performed with a constant displacement rate of 1 mm/min. The strain was measured using an extensometer, and the YS, ultimate tensile strength (UTS), and elongation were determined from the recorded tensile data.

3 | TEST RESULTS AND DISCUSSION

3.1 | Microstructural analysis

The microstructural features in different regions of the ER70S-6WAAM wall were investigated and the results are presented in Figure 3. A variation in the microstructure can be observed from the area in the vicinity of the fusion zone (FZ) and in the center of the melt pool. It was observed that the microstructure found within the melt pool was typically ferrite, which appeared as a polygon, with retained low volume fraction of pearlite phase formed along the grain boundaries of ferrite (see Figure 3A,C). The same microstructural features were reported in the previous studies by other researchers.[13,28] Higher magnification images along the melt-pool boundaries reveal Widmanstätten ferrite along with carbides. This type of microstructure is a result of remelting of the previously deposited layer during the process of overlapping layers, resulting in different thermal histories.[29]

Due to the higher cooling rates experienced in the fusion boundaries compared to the center of the melt pool, the formation of acicular ferrite was observed adjacent to the fusion lines (see Figure 3B,D). The transition of polygonal ferrite to acicular ferrite from the center of the melt pool to the side of the melt pool can be justified due to faster cooling rates in WAAM ER70S-6.[30] A detailed analysis of the microstructure conducted by Rafieazad et al.[13] revealed approximately 12.54% ± 0.56% volume of pearlite due to the low-carbon content in ER70S-6 feedstock. The welded structure of API-X70 has also revealed the presence of acicular ferrite and bainitic microstructure which is commonly welded using ER70S-6 filler wire.[13] The bainitic microstructure offers higher strength and toughness due to its smaller grain size and higher dislocation density as it provides obstacles to dislocation movement compared to polygonal ferrite.[31] This kind of microstructure was seen repeatedly and is dependent on the sequence of layer deposition. However, the complex thermal history which changes along the build direction also induces inhomogeneous

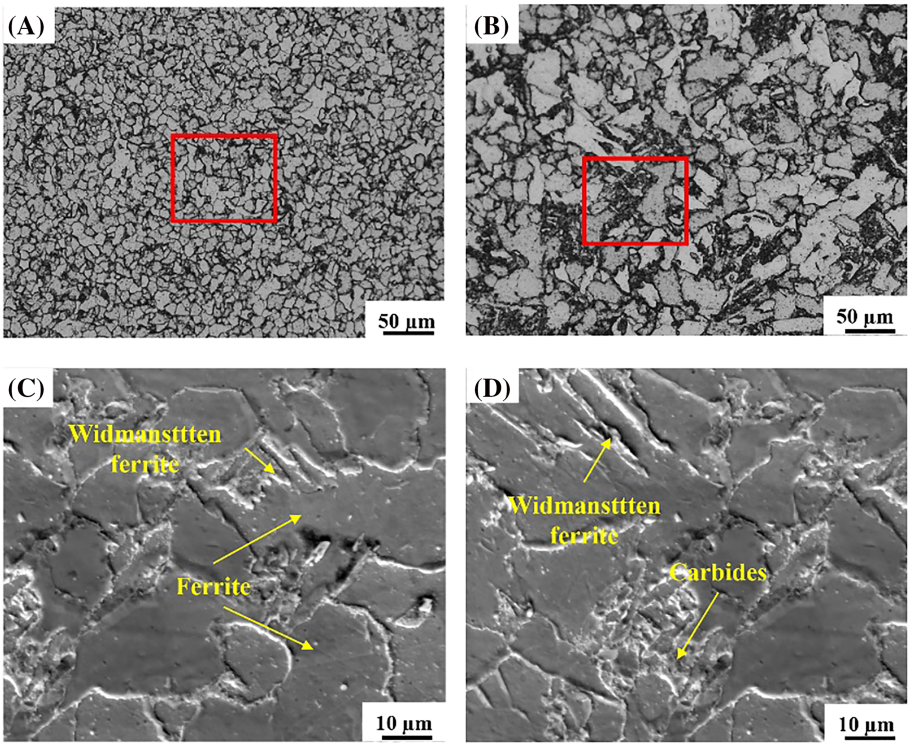

FIGURE 3 Optical microscopy images taken at different locations of the ER70S-6 WAAM wall (A) melt pool, (B) close to the fusion zone and center of the melt pool, (C) higher resolution SEM image of the enclosed area shown in (A), and (D) higher resolution SEM image of the enclosed area in (B) showing Widmanstätten ferrite and carbides [Colour figure can be viewed at wileyonlinelibrary.com]

microstructure along the built direction (i.e., Z axis in Figure 2B) of the wall.

The grain size is considered one of the most important microstructural characteristics that affects the mechanical properties of the component. The grain size distribution was therefore analyzed on the WAAM wall and presented in Figure 4 in the form of statistical distribution in three different regions of the wall: top, middle, and bottom. The grain size coarsening in the middle of the wall was observed and is represented in Figure 4. The higher distribution of smaller grain size can be observed at the bottom and the top of the wall. Considering the layer-by-layer deposition, the associated thermal cycles introduced into the material resulted in the grain growth in the vicinity of melt-pool geometry. Austenizing could be the main reason for grain growth in the middle of the wall as it was subjected to alternating thermal cycles. Higher cooling rates were responsible for smaller grains at the bottom of the wall. The absence of multiple thermal cycles at the top of the WAAM wall resulted in fine grain size as there were no alternating heating and cooling causing austenization of the grains. Such microstructural inhomogeneities between the layers and along the build direction could introduce mechanical anisotropy in the material.

3.2 | Micro-hardness analysis

The micro-hardness tests were conducted using 0.3 kg ($Hv_{0.3}$) and 10 kg (Hv_{10}) loads, and the results are shown in Figure 5A. While the hardness tests at the lower load characterized the local properties of the WAAM wall, the values obtained from the tests at the higher load (Hv_{10}) provided relatively more global response of the material by indenting a number of grains in each indentation. The results in Figure 5A show that similar hardness variations trends are obtained under both load levels, though the global values at the higher load are slightly lower than those obtained from the hardness tests under the lower load. It can be observed in Figure 5A that hardness values are generally higher near the bottom and top of the WAAM wall. This nonuniform micro-hardness variation along the build direction (i.e., along Z axis) depicts the anisotropic behavior of the build which is inherent in the WAAM process.

The maximum hardness recorded at $Hv_{0.3}$ was approximately 190 Hv and was closer to the top of the wall. Similar results were reported on ER70S-6 WAAM wall fabricated using the oscillation strategy by Ermakova et al.[14] Further micro-hardness testing along the wall thickness (i.e., along Y axis), illustrated in Figure 5B, showed spikes of hardness values at the bottom and top of the wall with the average hardness values of 168.8 ± 8 and 172 ± 10 at the top and bottom of the WAAM wall, respectively. The variation of the hardness values between the top, middle, and bottom of the wall is due to the difference in grain sizes which can be attributed to different thermal cycles during the deposition of the wall. The higher cooling rates experienced at these two locations promoted the formation of a higher distribution of smaller grains and Widmanstätten ferrite. The smaller grains offer higher strength and toughness due to higher dislocation density as it provides obstacles to dislocation movement compared to larger grains.

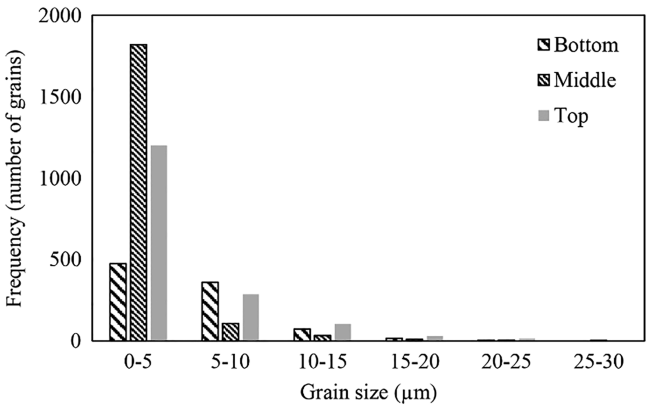

FIGURE 4 Statistical distribution of grain size variation at the bottom, middle, and top of the WAAM wall

3.3 | Tensile testing and analysis

The average results from tensile tests on three uniaxial specimens with both horizontal and vertical orientations are presented in Figure 6 and Table 2. Figure 6 shows the average "engineering stress *versus* engineering strain" curves in each orientation for parallel deposition strategy conducted in this study and oscillation deposition strategy taken from the literature.[14] Comparing the two deposition strategies, parallel-built samples showed slightly lower YS and UTS values which could be associated with the change in the material microstructure due to the difference in cooling rates in different deposition strategies. The influence of sample orientation on elongation, reported in the form of axial strain at failure $\varepsilon_{f,\ axial}$, can be observed in the horizontal and vertical samples for both deposition strategies. This mechanical anisotropy is linked with the difference in microstructure at different locations of the wall. The tensile test results show that both specimen orientation and deposition strategy would slightly influence the mechanical properties of ER70S-6 WAAM wall.

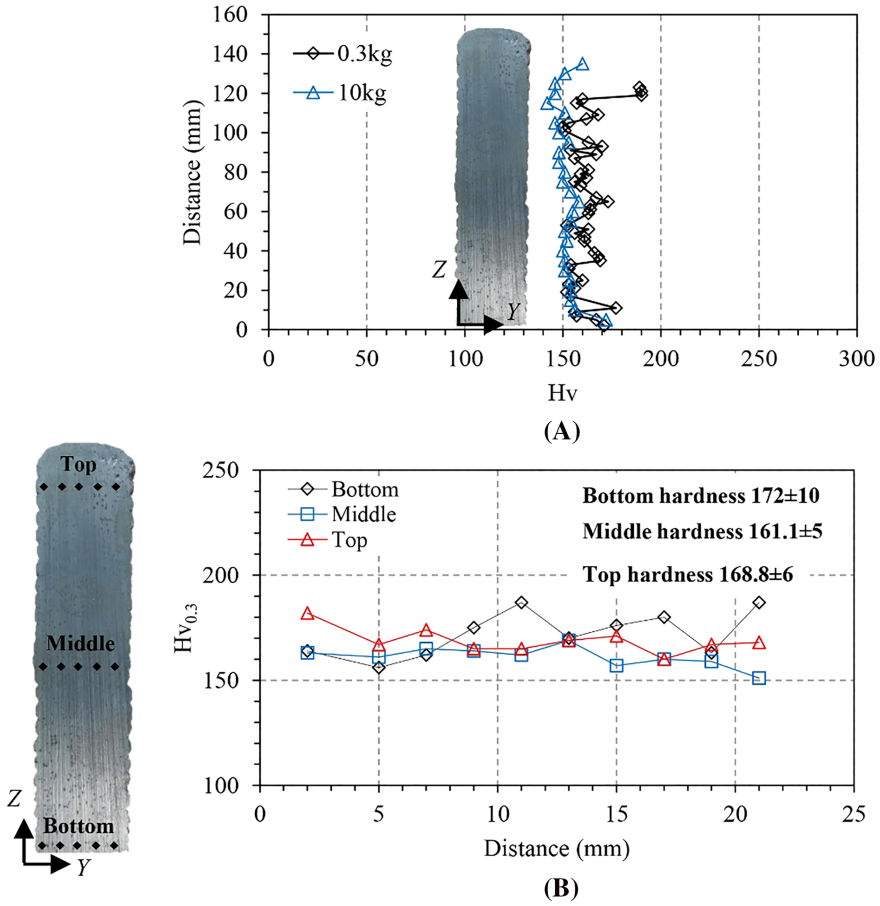

FIGURE 5 Hardness distribution of ER70S-6 WAAM wall (A) along the build direction and (B) along wall thickness [Colour figure can be viewed at wileyonlinelibrary.com]

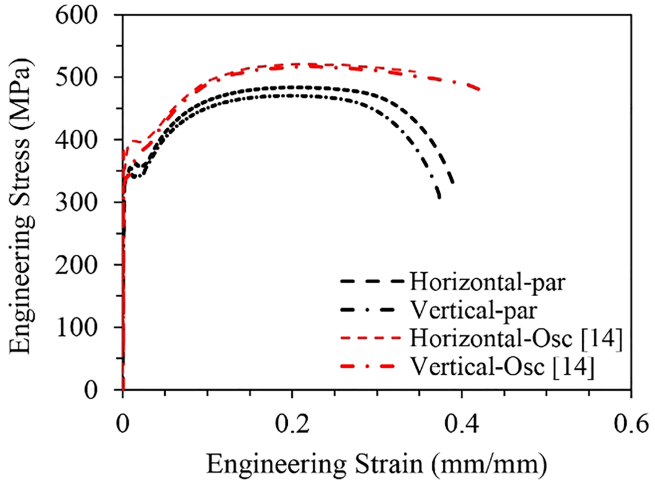

FIGURE 6 Tensile curves for parallel-built ER70S-6 WAAM wall from the present study compared to oscillation-built ER70S-6 WAAM wall taken from[14] [Colour figure can be viewed at wileyonlinelibrary.com]

3.4 | Fatigue crack propagation testing and analysis

For FCG analysis, four stepped-notch compact tension, C(T), samples were extracted from the WAAM wall. In order to examine the sample location and orientation effects on the FCG behavior of the material, C(T) samples were extracted along two different orientations (i.e., horizontal and vertical) and from two different locations (i.e., top and bottom of the WAMM wall) as schematically illustrated in Figure 2B. The C(T) samples with horizontal orientation taken from the top and bottom of the wall are designated as "Par-Top (H)" and "Par-Bottom (H)," respectively. Likewise, the C(T) samples with vertical orientation taken from the top and bottom of the wall are designated as "Par-Top (V)" and "Par-Bottom (V)," respectively. The C(T) samples for FCG testing were designed according to ASTM E647-15 standard[27] with the width of $W = 50$ mm, the height of $H = 60$ mm, and total thickness of $B = 16$ mm, with an initial machined crack length of $a_0 = 17$ mm before pre-fatigue cracking. Knife edges were also machined in the samples to enable the compliance measurements being carried out for crack length estimation as guided by ASTM E1820 standard.[32]

Load-controlled fatigue tests were carried out at room temperature on a 100 kN servo-hydraulic test machine under constant amplitude sinusoidal wave loading with a load ratio of $R = P_{min}/P_{max} = 0.1$, at 5 Hz frequency with maximum load of $P_{max} = 10$ kN and minimum load of

Material property	Parallel-built		Oscillation-built	
	Horizontal	Vertical	Horizontal	Vertical
YS (MPa)	318	347	390	365
UTS (MPa)	470	483	522	518
$\varepsilon_{f,\ axial}$ (mm/mm)	0.37	0.39	0.44	0.43

TABLE 2 Tensile properties from the parallel-built strategy in two different orientations compared with oscillation-built samples taken from[14]

$P_{min} = 1$ kN. Prior to fatigue testing, the samples were pre-cracked to approximately 20 mm (i.e., $a_{i,p}/W = 0.4$) under cyclic loading condition using decreasing load approach. During pre-cracking, it was ensured that the final value of the maximum stress intensity factor (SIF), K_{max}, did not exceed the initial K_{max} at the beginning of the actual FCG test.

The FCG tests were terminated when the crack length approached approximately 35 mm (i.e., $a_{f,p}/W = 0.7$). The SIF, K, for C(T) specimen geometry can be calculated using equation as suggested by ASTM E647 standard.

However, to address the validity concerns for C(T) samples with shallow crack lengths, Mehmanparast et al.[33] proposed a new shape function equation which is presented in Equation 1. This proposed equation is more accurate for calculation of K at a wider range of normalized crack lengths, ranging from $a/W = 0.2$ to $a/W = 0.7$.

$$K = \frac{P}{BW}.\sqrt{a}.\left(-372.12(a/W)^6 + 1628.60(a/W)^5 - 2107.46(a/W)^4 + 1304.65(a/W)^3 - 391.20(a/W)^2 + 54.81(a/W) + 7.57\right). \quad (1)$$

The crack length, a, versus the number of cycles, N, data from FCG tests are presented in the Figure 8A. The initial crack length of all the samples was 20 mm as shown in Figure 7A. In this figure, the crack growth trends for different orientations and locations are directly compared with each other. Similar crack growth trends were observed in all samples except for Par-Bottom (V) where some fluctuations in the crack growth behavior were observed at the beginning of the test. These fluctuations in the crack growth could be a result of crack diversion and bifurcation due to the localized microstructure and texture, which have been reported previously for other steels.[34] It has been observed in the literature that the presence of bainitic structure has been reported to slow down the crack growth rate that causes softening by dislocation rearrangement and annihilation during the strain-induced martensitic transformation.[35,36]

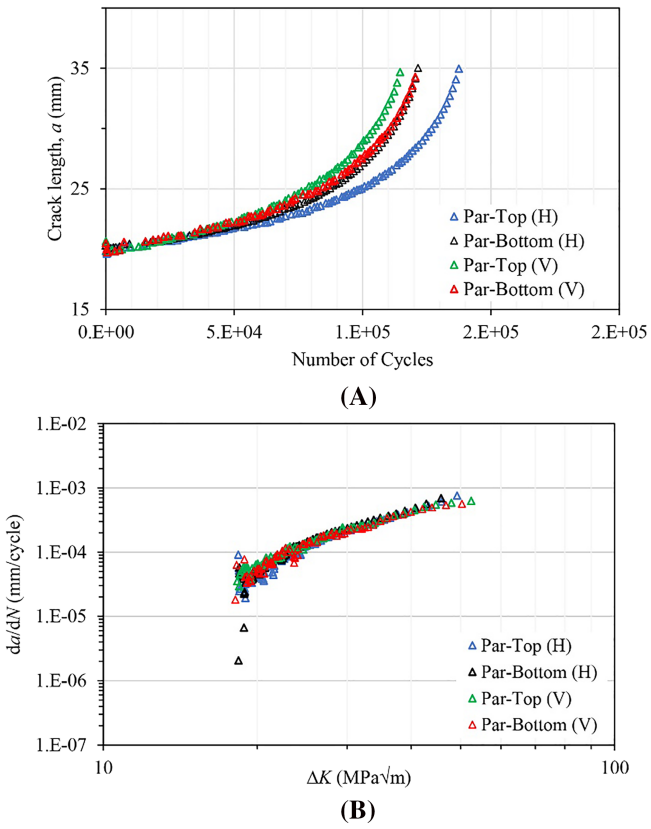

FIGURE 7 (A) "crack length *versus* number of cylces" data and (B) "crack growth rate *versus* stress intensity factor range" results [Colour figure can be viewed at wileyonlinelibrary.com]

The raw data from FCG tests were further analyzed to plot the FCG rate, da/dN, against the SIF range, ΔK, and the results are shown in Figure 7B. Following the guidelines provided in ASTM E647 standard, the FCG rates were calculated using the seven-point polynomial technique which provides more accurate rates compared to the secant method. The comparison of FCG rates in Figure 7B shows that for a range of ΔK values examined in the tests are within the inherent experimental scatter, similar FCG trends were obtained from specimens with different orientations and locations. It is worth noting that for a given location (i.e., top or bottom), only one test was performed on each specimen orientation. Therefore, more tests need to be conducted in future work to

TABLE 3 Paris law constants for the fatigue test results for the parallel-built strategy from the present study, compared to the ones obtained from the literature for the oscillation-built strategy[15] (the corresponding values for da/dN are in mm/cycle and ΔK in MPa$\sqrt{m}$)

Sample ID	Deposition strategy	Orientation	Location	C	m
Par-Top (H)	Parallel	Horizontal	Top	1.72×10^{-9}	3.42
Par-Bottom (H)	Parallel	Horizontal	Bottom	6.00×10^{-10}	3.77
Par-Top (V)	Parallel	Vertical	Top	1.13×10^{-8}	2.88
Par-Bottom (V)	Parallel	Vertical	Bottom	7.01×10^{-9}	3.01
CT-V-1	Oscillation	Vertical	Top	7.51×10^{-8}	2.39
CT-V-2	Oscillation	Vertical	Bottom	7.37×10^{-8}	2.39
CT-V-3	Oscillation	Vertical	Bottom	8.34×10^{-8}	2.99
CT-H-1	Oscillation	Horizontal	Top	4.29×10^{-9}	3.11
CT-H-2	Oscillation	Horizontal	Bottom	3.37×10^{-8}	2.59
CT-H-3	Oscillation	Horizontal	Top	2.80×10^{-9}	3.28

identify the level of scatter in each specimen location and orientation.

According to the Paris law, the FCG rate can be correlated with the fracture mechanics parameter ΔK using a power-law correction[37] which can be described as:

$$\frac{da}{dN} = C(\Delta K)^m, \tag{2}$$

where C and m are material constants. C and m values for the tests performed in this study were calculated from the Paris region and presented in Table 3. The values were calculated by plotting the line of best fit in the steady crack growth region and calculating the power-law constants. It was noted that the material constant, m, calculated in this study lies within the range of 2 to 4 which is typically observed in the wrought material counterparts tested in the absence of corrosive media.[15] From the results presented in Figure 8B and Table 3, it has been observed that the location and orientation of the C(T) samples do not have a major influence on the FCG behavior of the ER70S-6 WAAM specimen with parallel-built deposition strategy.

The FCG rates obtained from the present study were further compared with an oscillation-built deposition strategy on the same material from the literature.[15] The C(T) samples in Ermakova et al.[15] were tested in air at the same load ratio and P_{max}. The comparison of the parallel-built and oscillation-built strategies has been presented in Figure 8 and Table 3. It can be observed in Figure 8 that at relatively low values of SIF range (i.e., $\Delta K \leq 30$ MPa$\sqrt{m}$), the crack growth rates were slower for oscillation build samples. Also seen in Figure 8 is that the crack growth rates are almost identical for both deposition strategies for the SIF range of $30 \leq \Delta K \leq 40$ MPa$\sqrt{m}$, beyond which the oscillation-built

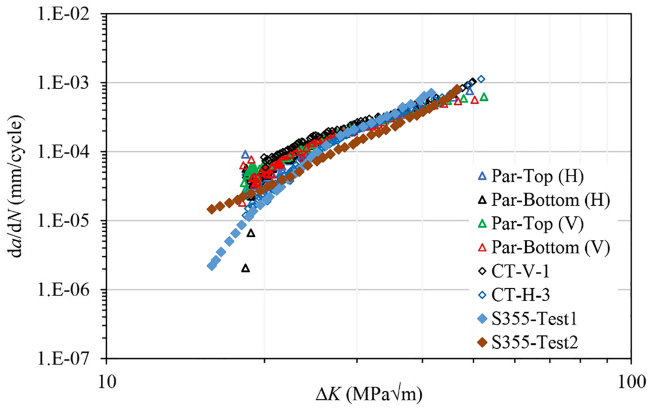

FIGURE 8 Comparison of FCG rates for the parallel-built strategy from the present study and the oscillation-built strategy from the lietrature[15] [Colour figure can be viewed at wileyonlinelibrary.com]

FCG rates become slightly higher at larger values of ΔK (i.e., $\Delta K \geq 40$ MPa$\sqrt{m}$) and towards the end of the tests. This is an opposite trend that was reported in the case of Ti64 by Syed et al.[22] who showed that slower FCG rates in oscillation-built Ti64 was obtained compared to parallel-built strategy. As explained in Syed et al,[22] the resultant microstructure of the oscillation-built reduced the YS of titanium alloy which in turn increased crack tip plasticity and crack deflection hence reducing the crack growth rates. In the present study, the difference in cooling rates does not seem to considerably affect the microstructure and YS of the mild carbon steel (ER70S-6); hence, the crack growth rate was not affected significantly by the build strategy. Overall, the crack growth rate has been found to be unaffected for both deposition strategies at different locations and orientations for ER70S-6. For further comparison, the crack growth rate

of S355 is also included in Figure 8. It can be observed FCG were slower in the base material.

4 | CRACK GROWTH PREDICTION IN WAAM-BUILT COMPONENTS

Jones et al.[38] modified the original Hartman–Schijve equation to the form of Equation 3 referred it as a variant of the NASGRO equation[38–41] because the constant q in the original NASGRO equation was set as $p/2$ in Equation 3.

$$\frac{da}{dN} = D\left(\frac{\Delta K - \Delta K_{thr}}{\sqrt{1 - K_{max}/A}}\right)^{p}. \quad (3)$$

In Equation 3 which is often referred to as Hartman–Schijve variant of NASGRO equation, K_{max} is the maximum value of SIF seen in a cycle, $\Delta K = (K_{max} - K_{min})$ is the range of the SIFs seen in a cycle, ΔK_{thr} is the "effective fatigue threshold," A is the cyclic fracture toughness, and D and p are material constants. The term ΔK_{thr} in Equation 3 is related to the ASTM E647 fatigue threshold ΔK_{th}, which is defined as the value ΔK corresponding to a crack growth rate, da/dN, equal to 10^{-10} m/cycle.

As illustrated in previous studies,[41–46] it appears that the variability in crack growth in addictively manufactured components can often be modeled using the Hartman–Schijve crack growth equation.[38,44] In this work, Equation 3 was used to compute the variability in the crack growth histories associated with various tests. The crack growth histories of the samples listed in

TABLE 4 The values of the parameters used to compute the crack growth histories shown in Figure 9

Sample ID	D	p	ΔK_{thr} (MPa √m)	A (MPa√m)
Par-Top (H)	1.36×10^{-9}	1.72	11.0	100
Par-Bottom (H)	1.36×10^{-9}	1.72	10.2	100
Par-Top (V)	1.36×10^{-9}	1.72	10.0	100
Par-Bottom (V)	1.36×10^{-9}	1.72	10.2	100
CT-V-1	1.36×10^{-9}	1.72	9.0	100
CT-H-3	1.36×10^{-9}	1.72	13.0	83

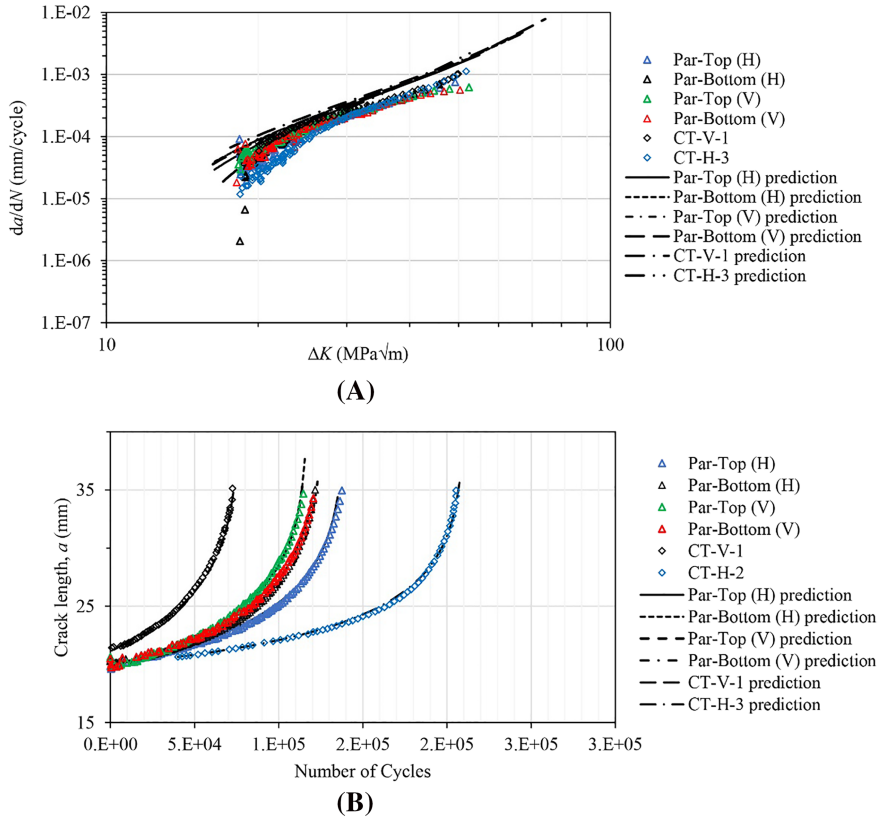

FIGURE 9 (A) Comparison between experimental data and predictions from Hartman–Schijve variant of NASGRO equation for da/dN versus ΔK curves and (B) comparison between measured and computed crack length for parallel and oscillation-built WAAM ER70S-6 at $R = 0.1$ [Colour figure can be viewed at wileyonlinelibrary.com]

Table 4 are shown in Figure 9A. The crack growth rate da/dN was plotted against $(\Delta K - \Delta K_{thr})/\sqrt{1 - K_{max}/A}$ in log–log axes as discussed in previous studies[42,43,47] where parameter A is the cyclic fracture toughness at fatigue failure. In the threshold region, da/dN is not sensitive to assume A values in the range of 80–100 MPa$\sqrt{m}$. The value of ΔK_{thr} was subsequently chosen to make da/dN versus $(\Delta K - \Delta K_{thr})/\sqrt{1 - K_{max}/A}$ plot and in the near threshold region appear as a straight line. The value of A was then adjusted to improve the linearity of the plot in the high ΔK region. This process generally results in slight difference in the da/dN versus $(\Delta K - \Delta K_{thr})/\sqrt{1 - K_{max}/A}$ plots in the high ΔK region. Hence, the value of A was estimated and is given in the Table 4.

A comparison between the measured and the computed crack growth histories for the parallel-built strategy WAAM specimens tested in this work and the oscillation-built strategy WAAM specimens from the literature is shown in Figure 9. Using Equation 3, fitted da/dN versus applied ΔK is presented in Figure 9A and compared with test measured crack growth data in Figure 9B. It can be seen that by allowing for variability in the fatigue threshold and the fracture toughness, reasonably good agreement is obtained between the experimental and computed results (see Figure 9B). The values of the parameters D and p used in this study are given in Table 4.

5 | CONCLUSIONS

This paper presents the systematic study on the influence of sample location and orientation of parallel-built deposition strategy ER70S-6 WAAM components on its microstructure, mechanical properties, and FCG rates. The key findings from this study are as follows:

1. The microstructure of the fabricated WAAM wall has two distinct regions across the melt pools, that is, polygonal ferrite and lamellar pearlite phases. Widmanstätten ferrite is observed at the melt-pool boundaries. The difference in temperature gradients and cooling rates has promoted the formation of these microstructural features.
2. The micro-hardness testing has revealed that the top and bottom regions of the wall have higher hardness values compared to the middle of the wall. The variation of hardness between the bottom, middle, and top of the wall is attributed to the difference in thermal cycles and associated with cooling rates promoting a higher distribution of smaller grains at the top and bottom of the WAAM wall.
3. The sample location and orientation do not have any significant impact on the FCG behavior of the ER70S-6 WAAM samples with parallel-built deposition strategy and the crack growth rates seem to be same at different locations and orientations of the WAAM wall.
4. Similar crack growth rates were found in the samples with parallel-built and oscillation-built deposition at the intermediate ΔK region; however, the oscillation-built specimens exhibit slightly higher FCG rates at larger values of ΔK.
5. The crack growth rate versus SIF range was computed using Hartman–Schijve variant of NASGRO equation, and the crack growth a versus number of cycles N was predicted. The variability in the crack growth histories can be reasonably well captured by using the Hartman–Schijve crack growth equation and allowing for variability in the fatigue threshold and the cyclic fracture toughness.

ACKNOWLEDGMENT

This work was supported by the Supergen ORE Hub Flexible Funding under Grant EP/S000747/1 from the UK Engineering and Physical Sciences Research Council (EPSRC).

AUTHOR CONTRIBUTIONS

Muhammad Shamir: Methodology; validation; formal analysis; writing-original draft. **Victor Igwemezie:** Formal analysis; writing-review and editing. **Saeid Lotfian:** Formal analysis; writing-review and editing. **Rhys Jones:** Methodology; validation; writing-original draft. **Huzaifa Asif:** Writing-review and editing. **Supriyo Ganguly:** Resources; writing-review and editing. **Ali Mehmanparast:** Conceptualization; resources; writing-review and editing; supervision.

DATA AVAILABILITY STATEMENT

The data that support the findings of this study are available on request from the corresponding author. The data are not publicly available due to privacy or ethical restrictions.

NOMENCLATURE

A	cyclic fracture toughness
a_0	initial crack length in C(T) specimen
$a_{f,c}$	final crack length (compliance data)
a_i	instantaneous crack length
$a_{i,p}$	crack length after pre-fatigue cracking
B	C(T) specimen thickness
C	material constant for fatigue crack growth
D	material constant in modified Hartman–Schijve equation

da/dN	fatigue crack growth rate
H	C(T) specimen height
K	stress intensity factor
K_c	fracture toughness
K_{max}	maximum stress intensity factor
K_{th}	threshold stress intensity factor for long crack
m	material constant for fatigue crack growth
p	material constant in modified Hartman–Schijve equation
P_{max}	maximum load
P_{min}	minimum load
R	load ratio
W	C(T) sample width
ΔK	stress intensity factor range
$\varepsilon_{f,\ axial}$	axial strain at failure

ORCID

Rhys Jones https://orcid.org/0000-0003-3197-2796

REFERENCES

1. Romano S, Brandão A, Gumpinger J, et al. Comparative study of fatigue properties of Ti-6Al-4V specimens built by electron beam melting (EBM) and selective laser melting (SLM). *Metall Mater Trans A*. 2018;131:102638.
2. Leuders S, Thöne M, Riemer A, et al. On the mechanical behaviour of titanium alloy TiAl6V4 manufactured by selective laser melting: fatigue resistance and crack growth performance. *Int J Fatigue*. 2013;48:300-307.
3. Chastand V, Quaegebeur P, Maia W, Charkaluk E. Comparative study of fatigue properties of Ti-6Al-4V specimens built by electron beam melting (EBM) and selective laser melting (SLM). *Mater Charact*. 2018;143:76-81.
4. Greitemeier D, Palm F, Syassen F, Melz T. Fatigue performance of additive manufactured TiAl6V4 using electron and laser beam melting. *Int J Fatigue*. 2017;94:211-217.
5. Fatemi A, Molaei R, Sharifimehr S, Phan N, Shamsaei N. Multiaxial fatigue behavior of wrought and additive manufactured Ti-6Al-4V including surface finish effect. *Int J Fatigue*. 2017;100:347-366.
6. Williams SW, Martina F, Addison AC, Ding J, Pardal G, Colegrove P. Wire + arc additive manufacturing. *Mater Sci Technol*. 2016;32(7):641-647.
7. Yehorov Y, da Silva LJ, Scotti A. Balancing WAAM production costs and wall surface quality through parameter selection: a case study of an Al-Mg5 alloy multilayer-non-oscillated single pass wall. *J Manuf Mater Process*. 2019;3(2):32.
8. Lockett H, Ding J, Williams S, Martina F. Design for Wire + Arc Additive Manufacture: design rules and build orientation selection. *J Eng Des*. 2017;1–31(7–9):568-598.
9. Dirisu P, Supriyo G, Martina F, Xu X, Williams S. Wire plus arc additive manufactured functional steel surfaces enhanced by rolling. *Int J Fatigue*. 2020;130:105237.
10. Paskual A, Álvarez P, Suárez A. Study on arc welding processes for high deposition rate additive manufacturing. *Procedia CIRP*. 2018;68:358-362.
11. DebRoy T, Wei HL, Zuback JS, et al. Additive manufacturing of metallic components—process, structure and properties. *Prog Mater Sci*. 2018;92:112-224.
12. Zhang J, Wang X, Paddea S, Zhang X. Fatigue crack propagation behaviour in wire+arc additive manufactured Ti-6Al-4V: effects of microstructure and residual stress. *Mater Des*. 2016;90:551-561.
13. Rafieazad M, Ghaffari M, Vahedi Nemani A, Nasiri A. Microstructural evolution and mechanical properties of a low-carbon low-alloy steel produced by wire arc additive manufacturing. *Int J Adv Manuf Technol*. 2019;105(5–6):2121-2134.
14. Ermakova A, Mehmanparast A, Ganguly S, Razavi J, Berto F. Investigation of mechanical and fracture properties of wire and arc additively manufactured low carbon steel components. *Theor Appl Fract Mech*. 2020;109:102685.
15. Ermakova A, Mehmanparast A, Ganguly S, Razavi J, Berto F. Fatigue crack growth behaviour of wire and arc additively manufactured ER70S-6 low carbon steel components. *Int J Fract*. 2021;104739.
16. Dirisu P, Ganguly S, Mehmanparast A, Martina F, Williams S. Analysis of fracture toughness properties of wire + arc additive manufactured high strength low alloy structural steel components. *Mater Sci Eng A*. 2019;765:138285.
17. Ermakova A, Mehmanparast A, Ganguly S. A review of present status and challenges of using additive manufacturing technology for offshore wind applications. *Procedia Struct Integr*. 2019;17:29-36.
18. The Crown State. Offshore Wind Operational Report 2020.
19. Ziegler L, Muskulus M. Lifetime extension of offshore wind monopiles: assessment process and relevance of fatigue crack inspection. In: *12th EAWE PhD Seminar*. DTU; 2016.
20. Haden CV, Zeng G, Carter FM, Ruhl C, Krick BA, Harlow DG. Wire and arc additive manufactured steel: tensile and wear properties. *Addit Manuf*. 2017;16:115-123.
21. Lu X, Zhou YF, Xing XL, Shao LY, Yang QX, Gao SY. Open-source wire and arc additive manufacturing system: formability, microstructures, and mechanical properties. *Int J Adv Manuf Technol*. 2017;93(5–8):2145-2154.
22. Syed AK, Zhang X, Davis AE, et al. Effect of deposition strategies on fatigue crack growth behaviour of wire + arc additive manufactured titanium alloy Ti–6Al–4V. *Mater Sci Eng A*. 2021;814:141194.
23. Syed AK, Zhang X, Caballero A, Shamir M, Williams S. Influence of deposition strategies on tensile and fatigue properties in a wire + arc additive manufactured Ti-6Al-4V. *Int J Fatigue*. 2021;149:106268.
24. ASTM International. *Standard Test Methods for Determining Average Grain Size Using Semiautomatic and Automatic Image Analysis 1*. ASTM International; 1997.
25. International Standard ISO. Metallic materials—Vicker's hardness test—Part 1: test method (ISO 6507-1:2018).
26. ASTM International. *Designation: E8/E8M − 16a Standard Test Methods for Tension Testing of Metallic Materials*. ASTM International; 2016.
27. ASTM International. *Standard Test Method for Measurement of Fatigue Crack Growth Rates*. ASTM International; 2016.
28. Colegrove PA, Coules HE, Fairman J, et al. Microstructure and residual stress improvement in wire and arc additively

manufactured parts through high-pressure rolling. *J Mater Process Technol*. 2013;213(10):1782-1791.
29. Zhang D, Liu A, Yin B, Wen P. Additive manufacturing of duplex stainless steels—a critical review. *J Manuf Process*. 2022;73:496-517.
30. Haselhuhn AS, Wijnen B, Anzalone GC, Sanders PG, Pearce JM. In situ formation of substrate release mechanisms for gas metal arc weld metal 3-D printing. *J Mater Process Technol*. 2015;226:50-59.
31. Bajaj P, Hariharan A, Kini A, Kürnsteiner P, Raabe D, Jägle EA. Steels in additive manufacturing: a review of their microstructure and properties. *Mater Sci Eng A*. 2020;772:138633.
32. ASTM International. *Designation: E1820—18a ϵ1 Standard Test Method for Measurement of Fracture Toughness*. ASTM International; 2019.
33. Mehmanparast A, Brennan F, Tavares I. Fatigue crack growth rates for offshore wind monopile weldments in air and seawater: SLIC inter-laboratory test results. *Mater Des*. 2017;114:494-504.
34. Igwemezie V, Mehmanparast A, Brennan F. The influence of microstructure on the fatigue crack growth rate in marine steels in the Paris Region. *Fatigue Fract Eng Mater Struct*. 2020;43(10):2416-2440.
35. Królicka A, Lesiuk G, Radwański K, et al. Comparison of fatigue crack growth rate: pearlitic rail versus bainitic rail. *Int J Fatigue*. 2021;149:106280.
36. Adamczyk-Cieślak B, Koralnik M, Kuziak R, Brynk T, Zygmunt T, Mizera J. Low-cycle fatigue behaviour and microstructural evolution of pearlitic and bainitic steels. *Mater Sci Eng A*. 2019;747:144-153.
37. Paris P, Erdogan F. A critical analysis of crack propagation laws. *J Basic Eng*. 1963;85(4):528-533.
38. Jones R, Molent L, Walker K. Fatigue crack growth in a diverse range of materials. *Int J Fatigue*. 2012;40:43-50.
39. Molent L, Jones R. The influence of cyclic stress intensity threshold on fatigue life scatter. *Int J Fatigue*. 2016;82:748-756.
40. Jones R, Raman RKS, Iliopoulos AP, Michopoulos JG, Phan N, Peng D. Additively manufactured Ti-6Al-4V replacement parts for military aircraft. *Int J Fatigue*. 2019;124:227-235.
41. Iliopoulos A, Jones R, Michopoulos J, Phan N, Singh Raman R. Crack growth in a range of additively manufactured aerospace structural materials. *Aerospace*. 2018;5(4):118.
42. Shamir M, Zhang X, Syed AK. Characterising and representing small crack growth in an additive manufactured titanium alloy. *Eng Fract Mech*. 2021;253:107876.
43. Jones R, Michopoulos JG, Iliopoulos AP, Singh Raman RK, Phan N, Nguyen T. Representing crack growth in additively manufactured Ti-6Al-4V. *Int J Fatigue*. 2018;116:610-622.
44. Jones R. Fatigue crack growth and damage tolerance. *Fatigue Fract Eng Mater Struct*. 2014;37(5):463-483.
45. Jones R, Rans C, Iliopoulos AP, Michopoulos JG, Phan N, Peng D. Modelling the variability and the anisotropic behaviour of crack growth in SLM Ti-6Al-4V. *Materials (Basel)*. 2021;14(6):1400.
46. Jones R, Kovarik O, Cizek J, Ang A, Lang J. Crack growth in conventionally manufactured pure nickel, titanium and aluminum and the cold spray additively manufactured equivalents. *Addit Manuf Lett*. 2022;3:100043.
47. Iliopoulos AP, Jones R, Michopoulos JG, Phan N, Rans C. Further studies into crack growth in additively manufactured materials. *Materials (Basel)*. 2020;13(10):5-10.

How to cite this article: Shamir M, Igwemezie V, Lotfian S, et al. Assessment of mechanical and fatigue crack growth properties of wire + arc additively manufactured mild steel components. *Fatigue Fract Eng Mater Struct*. 2022;45(10):2978-2989. doi:10.1111/ffe.13797

https://dspace.org/

Assessment of mechanical and fatigue crack growth properties of wire+arc additively manufactured mild steel components

Shamir, Muhammad; Igwemezie, Victor C.; Lotfian, Saeid; Jones, Rhys; Asif, Huzaifa ...

2022-07-20
Wiley
https://doi.org/10.1111/ffe.13797
Shamir M, Igwemezie V, Lotfian S, et al., (2022) Assessment of mechanical and fatigue crack growth properties of wire+arc additively manufactured mild steel components. Fatigue and Fracture of Engineering Materials and Structures, Volume 45, Issue 10, October 2022, pp. 2978-2989

Downloaded from a DSpace repository. https://dspace.org/